Article

Three-dimensional conductive conjugated polyelectrolyte gels facilitate interfacial electron transfer for improved biophotovoltaic performance

Zhongxin Chen[1,7], Samantha R. McCuskey [2,3,7], Weidong Zhang [1,4,5], Benjamin Rui Peng Yip [1], Glenn Quek[1], Yan Jiang [1], David Ohayon [1], Shujian Ong [6], Binu Kundukad [3], Xianwen Mao[1,4,5] & Guillermo C. Bazan [1,2] ✉

Living biophotovoltaics represent a potentially green and sustainable method to generate bio-electricity by harnessing photosynthetic microorganisms. However, barriers to electron transfer across the abiotic/biotic interface hinder solar-to-electricity conversion efficiencies. Herein, we report on a facile method to improve interfacial electron transfer by combining the photosynthetic cyanobacterium *Synechococcus elongatus* PCC 7942 (*S. elongatus*) with a conjugated polyelectrolyte (CPE) atop indium tin oxide (ITO) charge-collecting electrodes. By self-assembly of the CPE with *S. elongatus*, soft and semitransparent *S. elongatus*/CPE biocomposites are formed with three-dimensional (3D) conductive networks that exhibit mixed ionic-electronic conduction. This specific architecture enhances both the natural and mediated exoelectrogenic pathway from cells to electrodes, enabling improved photocurrent output compared to bacteria alone. Electrochemical studies confirm the improved electron transfer at the biotic-abiotic interface through the CPE. Furthermore, microscopic photocurrent mapping of the biocomposites down to the single-cell level reveals a ~ 0.2 nanoampere output per cell, which translates to a 10-fold improvement relative to that of bare *S. elongatus*, corroborating efficient electron transport from *S. elongatus* to the electrode. This synergistic combination of biotic and abiotic materials underpins the improved performance of biophotovoltaic devices, offering broader insights into the electron transfer mechanisms relevant to photosynthesis and bioelectronic systems.

Biophotovoltaics (BPVs) harness photosynthetic biocatalysts—such as enzymes, thylakoid membranes, oxygenic cyanobacteria, anoxygenic purple sulphur and non-sulphur bacteria, or algae—to convert solar energy into electrical power[1–5]. In particular, living BPVs that employ intact microorganisms like cyanobacteria and algae have gained substantial attention due to their inherent self-renewing capabilities[6–10]. Despite the theoretically high quantum efficiency of intracellular light-harvesting photosystems, i.e. greater than 90%, the overall solar-to-electricity conversion efficiency in whole-cell devices remains relatively low, typically below 1%[11–13]. This limitation arises in

A full list of affiliations appears at the end of the paper. ✉e-mail: chmbgc@nus.edu.sg

part from the lack of efficient electron transport pathways from the photosynthetic microorganisms to the electrode surface, which ultimately hampers the effective extraction of electrons generated during photosynthesis[14,15]. Notably, exoelectrogenic cyanobacteria like *Synechocystis sp*. PCC 6803 can engage in both direct electron transfer (e.g., via microbial nanowires[16]) and mediated electron transfer, which involves endogenous or exogenous redox mediators[6,17], or even through microbial consortia[18]. Such processes emphasize the diversity of electron flow strategies in BPVs and highlight the need for more effective ways to harness the electrons generated by photosynthesis. Improving interfacial electron transfer (IET) at the microbe–electrode interface–whether via direct contact or mediator-facilitated pathways –remains a key challenge for realizing higher photocurrent and overall BPV performance[19].

Substantial efforts have been dedicated to facilitating the IET process across abiotic/biotic interfaces by employing artificial redox-active materials and electrode engineering strategies[2,20]. For instance, exogenous electron mediators like lipid-soluble quinones[6,21] and phenazines[22] can diffuse beyond the periplasmic space and interact closely with the photosynthetic apparatus, facilitating electron extraction from cells[14,23,24]. Ferri/ferrocyanide $[Fe(CN)_6]^{3-}/^{4-}$, which is relatively lipid-insoluble, primarily accepts electrons from the periplasmic space of cyanobacteria[25]. Meanwhile, coating electrodes with interfacial nanomaterials has emerged as an effective approach to reduce electron transport resistance[26]. For example, studies have demonstrated that polymers containing electroactive osmium centers can serve as an electron transport network between photosynthetic microorganisms and electrodes, thereby enhancing photocurrent[27]. Similarly, quinone-[28] and ferrocene-containing polymers[29], carbon nanotubes[30], as well as organic semiconductors[31–33], have been found to enhance photocurrent by improving the electron transfer pathway at the interface. In particular, polypyrrole (PPy)-[34], polyaniline (PANI)-[35,36], polydopamine (PDA)-[5,37], and poly(3,4-ethylenedioxythiophene) (PEDOT)-functionalized[38–41] matrices have provided stable and conductive interfaces that enhance current extraction from photosynthetic cells and membranes. In these cases, the electrode is modified with polymers through electropolymerization, vapor-phase deposition, or simple coating, followed by subsequent addition of the biological element. Alongside these electrode surface modifications, engineering the material and architecture of electrodes offers yet another approach to enhancing IET[42]. Electrodes with rough surfaces, such as carbon felt and graphite, exhibit greater affinity for microorganism attachment compared to smooth surfaces like copper, platinum, and tin oxide[2]. Recent advancements also include the development of porous or hierarchical indium tin oxide (ITO) electrodes with high dimensionality and optical transparency for increasing the electroactive surface area available to cells without hindering their photosynthetic activity[6,43,44].

Conjugated polyelectrolytes (CPEs)–characterized by electronically delocalized backbones bearing ionic functionalities–offer a distinct and promising strategy to enhance electron transfer efficiency and overall device performance[45–47]. Previous studies have shown that CPEs can spontaneously self-assemble with electroactive *Shewanella oneidensis* MR-1 to form three-dimensional (3D) living composites that not only facilitate efficient charge transport for charge extraction or injection in microbial electrochemical cells but also accommodate higher bacterial loading[45,48]. These abiotic/biotic composites leverage a synergetic effect, with the encapsulated bacteria upregulating energy metabolism genes and their extracellular biomaterials enhancing the structural cohesion of the CPE[49].

In this work, we demonstrate a method to improve the photocurrent of living BPV systems by encapsulating the photosynthetic cyanobacterium *Synechococcus elongatus* PCC 7942 (*S. elongatus*) within a conductive and biocompatible CPE matrix (Fig. 1a). A highly p-doped CPE, namely PEDOT-S, is employed to form a 3D network with

inter-chain connectivity (Fig. 1b) in Blue Green medium (BG11, bacteria culture medium; see the Methods for the detailed composition), while maintaining sufficient optical transparency for photosynthesis. The self-assembled biocomposite system amplifies photocurrent output in a photoelectrochemical cell by enhancing extracellular electron transfer to the electrode (Fig. 1c). Furthermore, photocurrent mapping down to the single cell level demonstrates the enhanced electron transfer capabilities of individual cells facilitated by the PEDOT-S matrix.

Results
Characterizations and properties of PEDOT-S
PEDOT-S was obtained via a one-step polymerization from the monomer sodium 4-((2,3-dihydrothieno[3,4-*b*][1,4]dioxin-2-yl)oxy) butane-1-sulfonate (EDOT-S) using iron sulfate ($FeSO_4$) and ammonium persulfate ((NH_4)$_2S_2O_8$) as oxidants[50]. Gel permeation chromatography (GPC) revealed a molecular weight of approximately 4700 Da, corresponding to an average of ≈16 repeat units per polymer chain, aligning with values reported in the literature[51]. As shown in Fig. 2a, PEDOT-S as obtained immediately after synthesis demonstrates low absorption in the visible spectrum (400–700 nm) and significant polaronic absorption above 1000 nm (Figs. 2a and S6), indicative of a high degree of doping[50].

The relationship between the optical absorption of PEDOT-S and the degree of doping was elucidated by interactions with acidic and basic environments[52,53]. As shown in Fig. S7, aqueous sodium hydroxide (NaOH) treatment led to distinct absorption peaks at 585 nm (neutral) and 990 nm (polaronic), with a decrease in absorption beyond 1200 nm (bipolaron absorption), in accordance with a de-doping process. Subsequent addition of H_2SO_4 increased the absorption beyond 1000 nm, confirming that the doping process is reversible. These findings are supplemented by spectroelectrochemical experiments[54] that imposed decreasing potential from −0.6 V to 0.6 V, leading to decreased absorption of the neutral state (Fig. S8), illustrating the doping process. Electron paramagnetic resonance (EPR) spectroscopy of pristine PEDOT-S revealed the presence of radical species (Fig. S9), further supporting a p-doped state[51]. In this system, not only does p-doping facilitate low absorption in the visible light range, but also increases the presence of charge carriers, thereby facilitating electron transport[47] within biophotovoltaic systems.

The electrochemical properties of PEDOT-S were assessed using a three-electrode electrochemical cell. Cyclic voltammetry (CV) was performed on PEDOT-S in BG11 (medium for cyanobacterium *S. elongatus*), using an Ag/AgCl reference electrode. CV profiles displayed reversible and quasi-rectangular traces, indicative of a pseudocapacitive characteristic (Fig. 2b)[55]. The onset oxidation potential at −0.24 V corresponds to the polaron formation within the PEDOT-S structure. The low oxidation potential implies that the CPE will be predominantly p-doped at positive potentials, which makes PEDOT-S an effective electron acceptor[56], ultimately facilitating efficient electron transfer from the photosynthetic bacteria to PEDOT-S. Furthermore, the electrochemical stability of PEDOT-S was confirmed over 200 cycles (Fig. S10), demonstrating its potential for sustained electron transport in bioelectronic systems.

Optical transmittance is a critical factor as light penetration is essential for the photosynthetic activity of cells[44]. To quantify the optical transmittance, spectrophotometric analysis was conducted on PEDOT-S in BG11. An optical path length of 600 μm was used to approximate the thickness of biocomposites in the photocurrent measurements. We focused on the 400–500 nm (Soret band) and 600–700 nm (Q_y band) regions, corresponding to key chlorophyll absorption bands (Fig. S11)[57]. From Figs. 2c and S12, 0.5 mg mL^{-1} PEDOT-S allowed for over 80 % transmission across the key absorption ranges. Increasing the concentration to 2 mg mL^{-1} and 5 mg mL^{-1} reduced transmittance to approximately 45% and 25%, respectively.
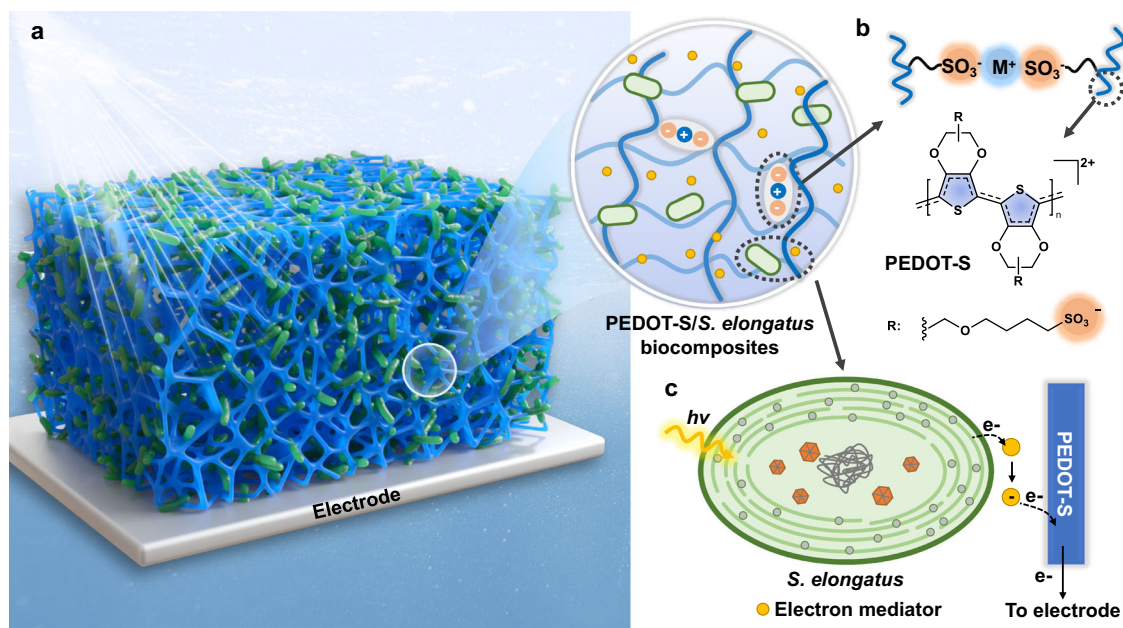
Fig. 1 | *S. elongatus*/PEDOT-S biocomposites form a 3D conductive matrix for efficient electron extraction. a Schematic of the *S. elongatus*/PEDOT-S bio-composite, depicting a conductive matrix (PEDOT-S, in blue color) encapsulating cyanobacterium *S. elongatus* (in green color). The PEDOT-S forms a 3D conductive network, allowing for efficient electron transport throughout the system. The zoomed-in schematic highlights the formation of a polymer network via interchain interactions. **b** Molecular structure of PEDOT-S, with the p-doped conjugated backbone (colored in blue) and the negatively charged chains (colored in orange). The PEDOT-S gel is expected to form through interchain connections via hydro-phobic effects and ionic interactions between the negatively charged sulfonate groups and positively charged counter ions. **c** Cartoon schematic representation of the electron transport pathway in the *S. elongatus*/PEDOT-S biocomposites. Electrons are generated by the photosynthetic activity of *S. elongatus* and are trans-ferred to a redox mediator ($K_3[Fe(CN)_6]$, yellow spheres), which facilitates electron shuttling between the biological system and the PEDOT-S matrix. The PEDOT-S polymer then serves as the conductive medium that transports these electrons to an external electrode. The cartoon schematic represents some key components within the cyanobacterium: carboxysomes (orange hexagons), chromosomes (grey tangled lines), phycobilisomes (grey spheres), and thylakoids (light green con-centric curves).

These results quantify the optical semitransparency of PEDOT-S, par-ticularly within a spectral region vital for photosynthesis.

Of particular interest is that PEDOT-S exhibits viscoelastic prop-erties when dispersed in BG11. This feature aligns with the properties of other CPEs that assemble into 3D conductive hydrogel networks through interchain ionic cross-links and hydrophobic contacts (Fig. 1b)[45,58,59]. To assess the impact of concentration on the physical properties of PEDOT-S, we performed rheology measurements using a plate-cone geometry[60]. For these tests, PEDOT-S in BG11 at con-centrations of 1, 2, and 5 mg mL^{-1} were deposited onto the testing plate, and a frequency sweep was conducted in the linear viscoelastic region. From Fig. 2d, one observes that the elastic modulus (G′) and loss modulus (G″) display a linear and parallel relationship across the measured frequency (ω) range, with G′ consistently exceeding G″. In contrast, PEDOT-S in DI water at 2 and 5 mg mL^{-1} displayed a divergent trend in G′ and G″, with G″ exceeding G′ over some of the frequency ranges, indicating a viscous-dominating behaviour (Fig. S13). This comparison indicates the gel-like behavior of PEDOT-S in BG11 and confirms the formation of a cohesive and conductive matrix for encapsulating living cells onto the electrode (Fig. S14)[61,62].

The biocompatibility of PEDOT-S with *S. elongatus* was investi-gated before the formulation of biocomposites. We cultured *S. elon-gatus* ($OD_{730} = 0.2$, corresponding to $\approx 1.0 \times 10^8$ cells mL^{-1}) with PEDOT-S at concentrations from 0.5 mg mL^{-1} to 5 mg mL^{-1} in BG11 medium. These cultures were incubated at 30 °C under illumination for 4 days. Bacterial viability was subsequently quantified using colony-forming unit (CFU) counts on agar plates. The results revealed that after 4 days of illumination, CFU counts of all PEDOT-S concentrations exceeded the initial seeding levels, suggesting that the introduction of PEDOT-S does not compromise cell viability. Moreover, 2 mg mL^{-1} and lower exhibited no significant growth inhibition, whereas 5 mg mL^{-1} led to a

51 % CFU reduction compared to the bare *S. elongatus*, likely due to reduced light penetration (Fig. S15). Previous studies have also demonstrated that PEDOT-based materials do not inhibit PSII photo-synthetic efficiency of green algae and cyanobacteria over 72 h and 48 h, respectively[63]. Therefore, PEDOT-S in concentrations of 5 mg mL^{-1} and lower were deemed suitable for subsequent photo-electrochemical experiments with *S. elongatus*.

Fabrication of PEDOT-S/*S. elongatus* biocomposites and mor-phological studies
Living biocomposites were prepared by combining various con-centrations of PEDOT-S with the same initial *S. elongatus* loading of $OD_{730} = 0.9$ (corresponding to 4.5×10^8 cells mL^{-1}) in BG11 (pH = 7.1). To assess the electrochemical properties and photocurrent output, a three-electrode electrochemical cell was designed (Fig. S16). The PEDOT-S/*S. elongatus* biocomposites were confined atop an ITO glass working electrode using a silicone gasket with an exposed area of 2 cm^2 and an optimized thickness of 600 μm (Supplementary Note 1). The assembly was covered with a dialysis membrane (MWCO of 3.5 kDa) to ensure confinement while allowing ion exchange with the electrolyte.

The morphology of the bare *S. elongatus* and PEDOT-S/*S. elon-gatus* biocomposites at different concentrations (1, 2, and 5 mg mL^{-1}) atop ITO electrodes were examined using scanning electron micro-scopy (SEM) and confocal laser scanning microscopy (CLSM). SEM images of bare *S. elongatus*, as depicted in Fig. 3a and b, show non-uniform coverage of *S. elongatus* cells on the electrode surface. The *S. elongatus* cells tended to form small clusters in certain areas (Fig. S17), which may be associated with biofilm formation. Neat PEDOT-S shows a sheet-like and porous structure with irregular textures on the surface (Fig. S18) suggesting the three-dimensional network of the polymer. In the PEDOT-S biocomposites, cells were embedded within the
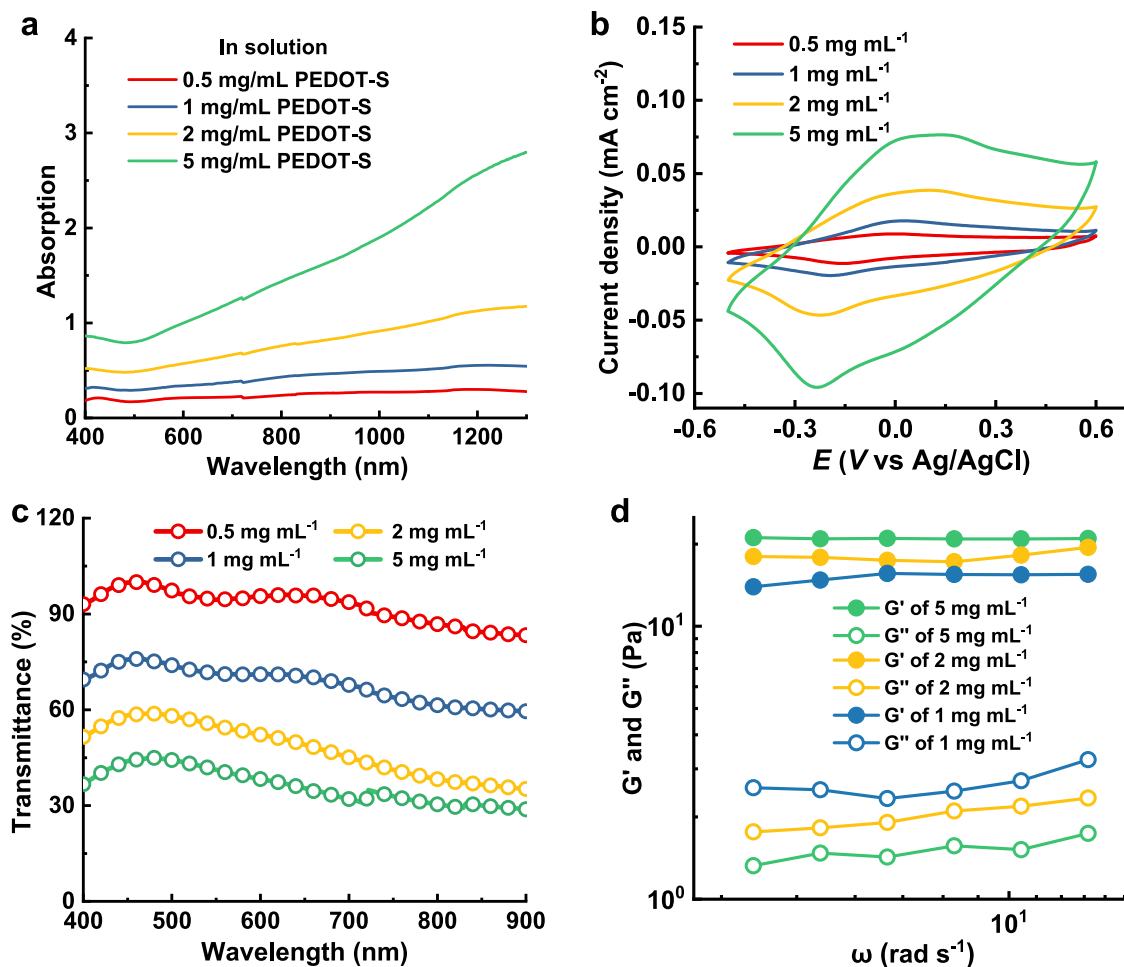
Fig. 2 | Optical and mechanical properties of PEDOT-S at various concentrations. a Absorption spectra in the visible to near-infrared range (400–1300 nm). **b** CV traces at a scan rate of 5 mV s^{-1} with BG11 as the electrolyte. **c** Transmittance (%) in the wavelength range of 400–900 nm. Absorption, transmittance, and CV spectra were measured atop ITO electrodes with 600 μm spacer thickness (optical pathlength) **d** Rheological measurements in BG11 depicting the elastic (G′) and loss moduli (G″) as a function of frequency (ω) at a constant strain of 0.01% and a temperature of 23 °C.

polymeric matrix (Figs. 3c, d, and S17), forming a thick agglomerated structure (Fig. 3e). As the PEDOT-S concentration increased, the polymer framework became progressively thicker (Fig. S19). CLSM analysis provides further insights into the in-situ spatial arrangement and distribution of *S. elongatus* utilizing the intrinsic fluorescence of the cells[57]. Specifically, *S. elongatus* cells exhibit intrinsic fluorescence from chlorophyll pigments at wavelength 650–750 nm when excited by 620 nm or 635 nm laser, whereas PEDOT-S does not emit fluorescence in this wavelength range (Fig. S20 and S21), allowing selective imaging of the cells. As shown in Fig. 3f, bare *S. elongatus* exhibited a thin and uneven biofilm layer with a limited vertical (z-axis) organization of less than 10 μm. For the PEDOT-S biocomposites, *S. elongatus* were dispersed within a larger 3D framework (Fig. 3g) with an enhanced z-axis spread around 30 μm, indicating a spatial distribution of the cells into the conductive PEDOT-S matrix. These observations suggest that the PEDOT-S matrix facilitates cell immobilization and supports a 3D architecture, which improves cell-electrode wiring and provides charge transfer pathways between cells and the electrode as shown in Fig. 3e and represented in Fig. 1a.

Photocurrent output facilitated by the PEDOT-S matrix

To evaluate the photocurrent production of PEDOT-S/*S. elongatus* biocomposites, we conducted chronoamperometry (CA) in electrochemical cells by applying a potential (E_{CA}) of 0.3 V (*vs* Ag/AgCl) under alternating dark and light conditions using a white LED light

(1 mW cm^{-2}, approximately 50 μmol photons m^{-2} s^{-1}). The living biocomposites were prepared by combining various concentrations of PEDOT-S with *S. elongatus* in BG11 media. The photocurrent density (J_{ph}) is defined as the difference in current density (J) between the endpoints of illuminated and dark conditions over a light on-off cycle[44]. Before measuring the photocurrent, biocomposites were kept in the dark at an E_{CA} of 0.3 V for 3 hours to facilitate cell attachment and minimize capacitive charges.

Photocurrent was first measured without the addition of an exogenous electron mediator (Fig. 4a). *S. elongatus* alone displayed a J_{ph} of 0.004 ± 0.001 μA cm^{-2}. After incorporating PEDOT-S at concentrations of 1 mg mL^{-1}, 2 mg mL^{-1}, and 5 mg mL^{-1}, the J_{ph} increased to 0.046 ± 0.004 μA cm^{-2}, 0.049 ± 0.015 μA cm^{-2}, and 0.091 ± 0.019 μA cm^{-2}, respectively (Fig. 4c). Notably, the 5 mg mL^{-1} PEDOT-S biocomposite demonstrated an over 20-fold J_{ph} increase compared to *S. elongatus* alone, suggesting enhanced electron transfer from *S. elongatus* to electrode through the conductive PEDOT-S matrix[45]. We then performed electrochemical impedance spectroscopy (EIS) to elucidate the electrochemical properties. In the Nyquist plots obtained from EIS measurements, characteristic semicircles at high frequencies denote charge transfer resistance (R_{CT}), with smaller diameters signifying more efficient charge transfer and current collection at the abiotic-biotic interface[64]. *S. elongatus* exhibits large impedance without a distinct semicircular shape (Fig. 4d), suggesting limited interfacial charge transfer. Increasing concentrations of PEDOT-S led to
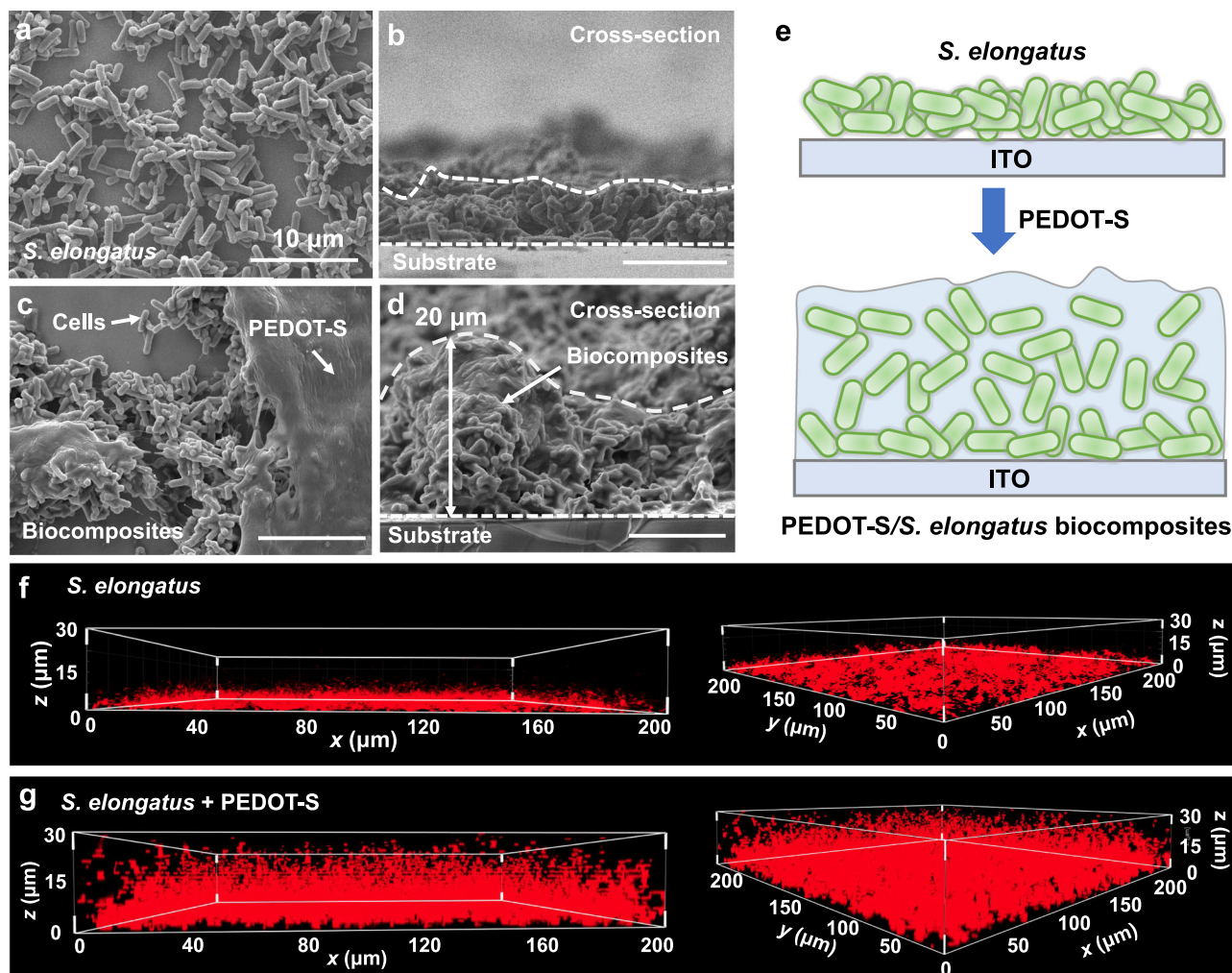
Fig. 3 | Microstructure of *S. elongatus* and PEDOT-S/*S. elongatus* biocomposites. **a**, **c** Representative scanning electron microscopy (SEM) images of *S. elongatus* and PEDOT-S/*S. elongatus* biocomposites after photocurrent collection in a photoelectrochemical experiment, respectively. The imaging experiments were independently repeated three times with similar results. **b**, **d** Cross-sectional SEM images of *S. elongatus* and the PEDOT-S/*S. elongatus* biocomposites, respectively. **e** Schematic representation of the microstructure of *S. elongatus* and PEDOT-S/*S. elongatus* biocomposites. **f**, **g** Z-stack imaging of *S. elongatus* and PEDOT-S/*S. elongatus* biocomposites at a depth of 30 μm performed using confocal laser scanning microscopy (CLSM), utilizing the intrinsic fluorescence of chlorophyll within the *S. elongatus* cells ($\lambda_{exc} = 620$ nm, $\lambda_{emi} = 650{-}750$ nm), which are shown as red dots.

decreased impedance and smaller semicircle diameters (Fig. 4d), suggesting that PEDOT-S serves as a conductive matrix to decrease the kinetic barriers for charge extraction.

To further investigate the mechanisms underlying photocurrent enhancement in the PEDOT-S biocomposites, we evaluated the electroactive surface areas (ESAs) to quantify the extent of the electrode that participates in electrochemical reactions (detailed calculations provided in Supplementary Note 2)[65]. For different PEDOT-S concentrations, we extracted the peak current responses of the $K_3[Fe(CN)_6]$ redox probe from CV profiles at varying scan rates, and then analyzed the data using the Randles-Sevcik equation[66]. Notably, 5 mg mL^{-1} PEDOT-S possesses an ESA of $6.20 \pm 0.81 \times 10^{-3}$ cm^2, over three times higher than the bare ITO control at $1.62 \pm 0.01 \times 10^{-3}$ cm^2 (Fig. 4e). This implies that the conductive network formed by PEDOT-S increases the number of active sites for redox processes, thereby enhancing charge extraction from the cells[45].

With the addition of 1 mM potassium ferricyanide ($K_3[Fe(CN)_6]$, midpoint potential at 0.20 V) as an exogenous redox mediator, the J_{ph} of *S. elongatus* was elevated to 0.14 ± 0.11 μA cm^{-2} (Fig. 4f), reflecting enhanced mediated electron transfer from the cells to the electrode surface[25]. Moreover, incorporating 1 mg mL^{-1} and 2 mg mL^{-1} PEDOT-S increased photocurrent to 0.21 ± 0.03 and 0.83 ± 0.07 μA cm^{-2},

respectively, indicating that PEDOT-S can also enhance mediated electron transfer processes[39]. However, further increasing the PEDOT-S concentration to 5 mg mL^{-1} lowered the J_{ph} to 0.16 ± 0.03 μA cm^{-2}.

To elucidate the behavior of the PEDOT-S biocomposites with the added mediator, EIS was performed to quantify the R_{CT} and the restricted diffusion resistance (R_d) by fitting the impedance spectra (Z) as a function of frequency (f) to an equivalent circuit model (Fig. 4g, see Methods for details)[59]. While the *S. elongatus* alone had an R_{CT} of 2500 ± 300 Ω cm^{-2}, introducing 1 mg mL^{-1}, 2 mg mL^{-1}, and 5 mg mL^{-1} PEDOT-S reduced R_{CT} to 500 ± 50 Ω cm^{-2}, 350 ± 50 Ω cm^{-2}, and 400 ± 50 Ω cm^{-2}, respectively (Figs. S22 and S23). Although 2 mg mL^{-1} and 5 mg mL^{-1} PEDOT-S biocomposites show relatively comparable R_{CT}, the R_d for the 2 mg mL^{-1} biocomposite is 2 ± 1 Ω cm^{-2}, significantly lower than the 150 ± 30 Ω cm^{-2} for 5 mg mL^{-1} biocomposites, signifying less diffusional hindrance. CV measurement provides further insights. *S. elongatus* and 1 mg mL^{-1} PEDOT-S biocomposites displayed similar redox peaks centered around 0.20 V originating from $K_3[Fe(CN)_6]$ (Fig. S24). The 2 mg mL^{-1} biocomposite shows higher and broader redox waves, attributed to enhanced pseudocapacitance characteristics resulting from higher PEDOT-S loading. This increased polymer loading fosters more continuous interchain contacts[55,67]. However, the 5 mg mL^{-1} PEDOT-S/*S. elongatus* biocomposite showed a lower peak
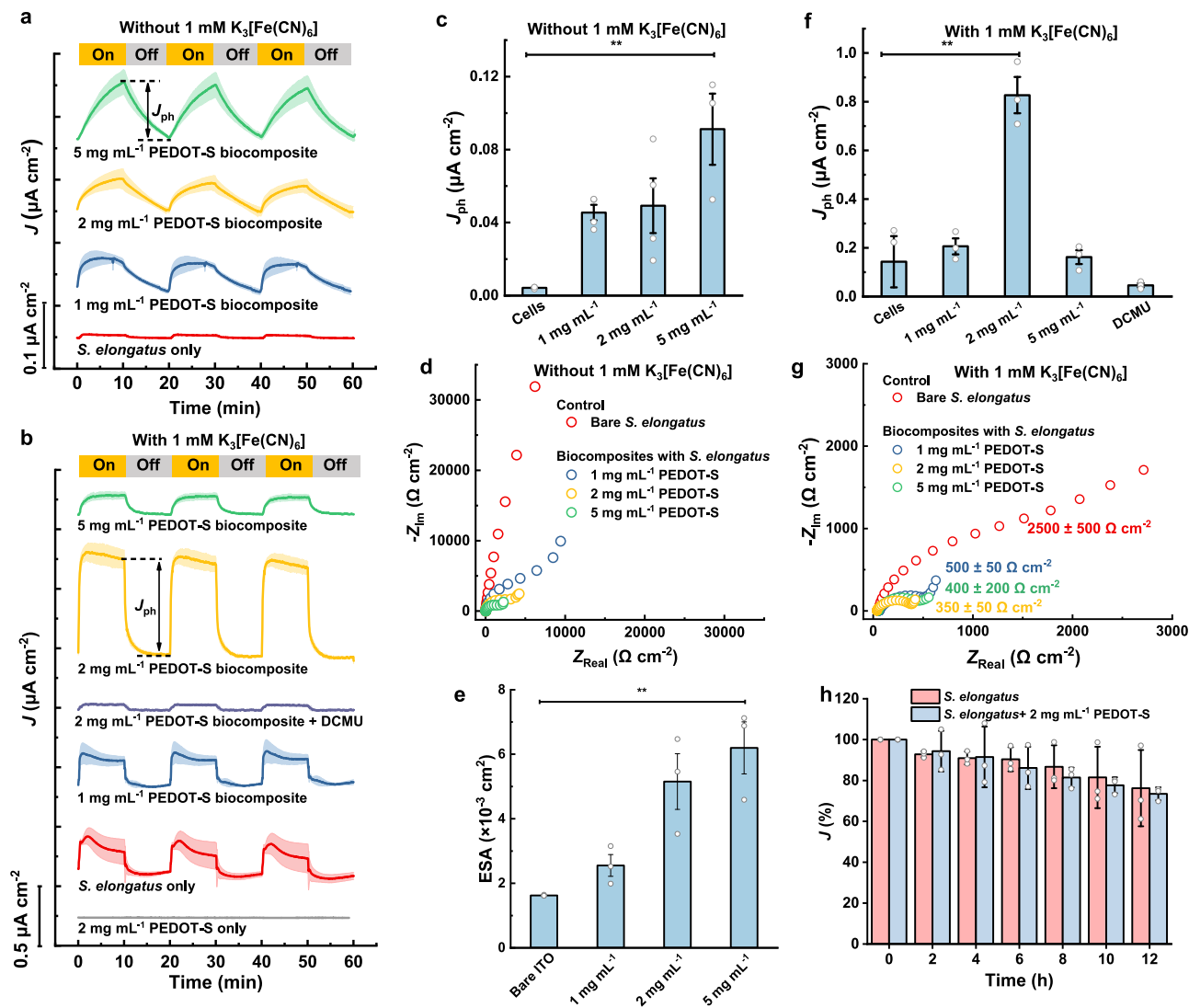
Fig. 4 | Photocurrent generation and electrochemical properties of PEDOT-S/S. *elongatus* **biocomposites. a, b** Chronoamperometry (CA) plots for *S. elongatus* and PEDOT-S/*S. elongatus* biocomposites under alternating light and dark conditions without and with the presence of 1 mM $K_3[Fe(CN)_6]$. The solid line shows the average current density while the shaded area represents the standard error of the mean ($n = 3$, biologically independent samples). The photocurrent density (J_{ph}) is defined as the difference in current between the light-on and light-off states. **c** Comparison of J_{ph} for *S. elongatus* alone and PEDOT-S/*S. elongatus* biocomposites under mediator-less conditions. The p-value for the comparison between bare cells and 5 mg mL^{-1} PEDOT-S/*S. elongatus* biocomposites is 0.009 (*$p < 0.05$, **$p < 0.01$). **d** Representative Nyquist plots for *S. elongatus* and PEDOT-S/*S. elongatus* biocomposites under mediator-less conditions. **e** Electroactive surface areas (ESAs) of bare ITO and PEDOT-S at various concentrations determined by CV analysis. The *p* value for the comparison between bare cells and 2 mg mL^{-1} PEDOT-S/*S. elongatus* biocomposites is 0.005 (*$p < 0.05$, **$p < 0.01$). **f** Comparison of J_{ph} for *S. elongatus*

and PEDOT-S/*S. elongatus* biocomposites under mediator conditions. The DCMU control experiments were performed on the 2 mg mL^{-1} PEDOT-S biocomposite samples. The p-value for the comparison between bare cells and 5 mg mL^{-1} PEDOT-S/*S. elongatus* biocomposites is 0.006 (*$p < 0.05$, **$p < 0.01$). **g** Representative Nyquist plots for *S. elongatus* and PEDOT-S/*S. elongatus* biocomposites under mediator conditions. The average charge transfer resistance (R_{CT}) values annotated were determined from equivalent circuit fitting. **h** Current density (J) over time from CA measurements for *S. elongatus* and PEDOT-S/*S. elongatus* biocomposites under continuous illumination over 12 hours. The data are shown as a percentage of the initial current output (J %). In all figures the error bars represent the standard error of the mean ($n = 3$, except 2 mg mL^{-1} in (**c**) $n = 4$, all are biologically independent samples). Statistical analysis was performed using one-way ANOVA followed by Tukey's Honestly Significant Difference (HSD) post-hoc test. All tests were two-sided, and *p* values were adjusted for multiple comparisons.

current and narrower redox wave compared to 2 mg mL^{-1}, consistent with the ion diffusion impedance. Collectively, these results suggest that while higher concentrations of PEDOT-S enhance the formation of a more conductive matrix, excessive concentrations can hinder the diffusional transport of redox mediators[68]. With the presence of 1 mM $K_3[Fe(CN)_6]$, 2 mg mL^{-1} PEDOT-S emerges as the optimal concentration to integrate with *S. elongatus* with the benefits of increased active sites for electron transfer while maintaining low diffusional resistance.

Cell loading capacity was investigated to examine the interaction between *S. elongatus* cells and the electrode by varying the bacterial cell density within the biocomposites. While bare ITO exhibited a clear

saturation in photocurrent when the *S. elongatus* loading reached 3.0×10^8 cell mL^{-1}, the 2 mg mL^{-1} PEDOT-S biocomposites displayed a linear relationship between photocurrent and bacterial loading up to 6.0×10^8 cell mL^{-1} (Fig. S25). This behavior indicates that cells within the biocomposite receive adequate light, and the polymer matrix effectively integrates the cells and facilitates a robust electronic connection between them and the electrode.

The specific involvement of photosynthetic activity in photocurrent production was further verified by the addition of 3-(3,4-dichlorophenyl)-1,1-dimethylurea (DCMU), an inhibitor of photosynthetic electron transport[32], to the 2 mg mL^{-1} PEDOT-S/*S. elongatus*

biocomposite. This led to a significant decrease in J_{ph} from 0.83 ± 0.07 to $0.05 \pm 0.01\,\mu A\ cm^{-2}$ (Fig. 4b and f). The controls of PEDOT-S + $K_3[Fe(CN)_6]$ and $K_3[Fe(CN)_6]$ without cells generated negligible photocurrent (Figs. 4b and S26), indicating that the abiotic components do not contribute to the photocurrent. Collectively, these findings confirm that the observed photocurrent was generated by the photosynthetic activity of *S. elongatus* and that the PEDOT-S conveys an advantage for electron extraction, leading to photocurrent improvement.

BPV systems are typically evaluated not only based on power output but also on operational stability under illumination[69,70]. Of relevance is that long-term operational stability is limited due to the inherent complexities of integrating living organisms with electronic components[25]. We monitored the output current density (*J*) every 2 hours, comparing it to the initial current output under light exposure (Fig. S27). Both *S. elongatus* and the 2 mg mL^{-1} PEDOT-S biocomposite retained over 70 % of their performance after continuous illumination for 12 hours (Fig. 4h), indicative of a sustained photocurrent output comparable with previous studies[6,7]. Sustained cell growth and ATP production after the experiment suggest that cell viability is maintained (Fig. S28).

Microscopic cell-electrode interactions demonstrated by single-cell photocurrent mapping

We performed electrochemical experiments down to single-cell levels to further demonstrate the electrochemical interaction between cells and the electrodes. We employed a multimodal microscopy platform to image and map the photocurrent of the biocomposites (Fig. S29)[71]. The use of single-cell photocurrent mapping allows us to disentangle the cell-electrode interactions in complex biological-electrode systems and provides a microscopic evaluation of the performance of biophotovoltaics. While methods such as CFU estimation provide an overall view of biocatalyst performance, they mask the heterogeneity in cell–electrode interactions—especially in polymeric networks. As normalizing photocurrent by bacterial number or chlorophyll content remains challenging for accurate performance evaluations, single-cell photocurrent mapping assisted by fluorescence microscopy offers an alternative method to evaluate the performance by directly measuring per-cell current outputs, revealing which cells are effectively "wired" to the electrode and how the polymer network influences electron generation/collection. Furthermore, single-cell measurements provide insight into the maximum electron transfer capabilities of individual cells, revealing design parameters such as interfacial materials or cell density that can optimize the performance of the system.

To perform single-cell photocurrent measurements, suspensions of 2 mg mL^{-1} PEDOT-S biocomposite and bare *S. elongatus* cells in the presence of 1 mM $K_3[Fe(CN)_6]$ were dispersed onto a fluorine-doped tin oxide (FTO) substrate within a photoelectrochemical microfluidic cell. The samples were confined using a transparent coverslip with a 100 μm spacer (Figs. 5a and S29). Before the photocurrent experiment, a soft agarose pad was gently pressed on top of the samples to ensure close contact between the bacteria and the electrode. This procedure was to flatten the sample into a thin layer, preventing cells from stacking above or below the focal plane and allowing accurate single-cell current measurements. Fluorescence imaging confirmed that both the bare bacteria and PEDOT-S biocomposite samples were arranged nearly as monolayers (Figs. S30 and S31), with no significant out-of-focus cell clusters in the detected areas.

To quantify the photocurrent at localized regions, we utilized a focused 405 nm laser to excite cells within areas approximately 20–30 μm in diameter. The *J* versus time (*J-t*) response under on-off light illumination was probed at $E_{CA} = 0.5\,V$ (versus Ag/AgCl). The focused light ensured that only the bacteria within the illuminated

regions contributed to the photocurrent. Upon light excitation, bare *S. elongatus* (bacteria number of 15) generated a J_{ph} of 0.28 ± 0.07 nA. In contrast, PEDOT-S biocomposites with the same cell count exhibited a J_{ph} approximately ten times higher, measuring 2.13 ± 0.19 nA (Fig. 5f). This increase suggests that PEDOT-S effectively facilitates charge transfer at the abiotic-biotic interface. By randomly illuminating different regions of the FTO substrate, J_{ph} measurements were taken for both bare *S. elongatus* and biocomposites across varying cell numbers (Figs. S32–S45). The PEDOT-S biocomposites showed a nearly linear increase in photocurrent with an increasing number of bacteria (Fig. 5g). This linearity suggests that the PEDOT-S conductive matrix promotes interfacial electron transfer capabilities of individual cells as well as consistent charge transfer across multiple cells. In contrast, the bare *S. elongatus* shows a much lower photocurrent with less dependence on cell count. This result is consistent with the bulk experiments, in which we observed a nearly linear increase of the photocurrent with increasing bacterial loading in the PEDOT-S matrix, while the bare *S. elongatus* shows an obvious saturation (Fig. S24). Normalizing the photocurrent to the number of cells shows that the per-cell J_{ph} of PEDOT-S biocomposites (0.18 ± 0.06 nA) was approximately tenfold higher than that of bare *S. elongatus* cells (0.018 ± 0.004 nA) (Fig. 5h). This enhancement in single-cell photocurrent suggests that the PEDOT-S biocomposite facilitates efficient interfacial electron transfer of individual cells.

Comparison of PEDOT-S matrix properties with previous studies

It is worth pointing out that a variety of PEDOT-based materials have been used previously in bioelectronics with the intent of improving the ability to harness the electrons of bacteria or photosynthetic microorganisms[38,39,41,61]. While many of these studies employ PEDOT:PSS or electrochemically deposited PEDOT films, our work utilizes a self-doped PEDOT-S, characterized by delocalized π-backbone bearing ionic alkyl chains. Such a structure not only provides water solubility and biocompatibility but also allows the formation of a soft 3D matrix through interchain ionic cross-links and hydrophobic contacts. The mixed ionic-electronic conduction of the gel facilitates charge transport under the mildly ionic conditions of photosynthetic cultures. Such properties are particularly relevant when compared to prior PEDOT coatings that rely on additional dopants or additives that can potentially reduce biocompatibility and electrochemical properties of the polymer.

In previous studies, coating electrodes with conductive polymers such as polyaniline, polypyrrole, or PEDOT-based materials has typically yielded improvements in photocurrent outputs on the order of two- to tenfold, depending on the microorganisms and specific polymer formulation[13,34,38,39,72]. In this study, we observed a more than 20-fold increase in photocurrent in the absence of a mediator and an approximately 6-fold increase in the presence of ferricyanide when PEDOT-S was integrated with *S. elongatus* compared to the bare cells. The increment in photocurrent is attributed to the increased ESA and low charge transfer resistance of the PEDOT-S network thus improving the cell–electrode interface and harnessing of photosynthetically generated electrons.

Compared to strategies focused on electrode architectures—such as inverse opal–indium tin oxide (IO-ITO)[6,73] or hierarchical pillar array ITO structures[44]—that enhance photocurrent output by engineering electrodes with porous or pillar-based surfaces, our approach focuses on improving cell–electrode communication. This is achieved by forming a soft, 3D polymer matrix that intimately connects individual cells to the electrode. These approaches are distinct yet complementary: incorporating conductive polymer and CPEs like PEDOT-S into high-surface-area architectures such as IO-ITO could further enhance cell loading and reduce charge transfer resistance, potentially leading to even greater photocurrent. Given the straightforward synthesis of PEDOT-S and the scalability and cost considerations of the
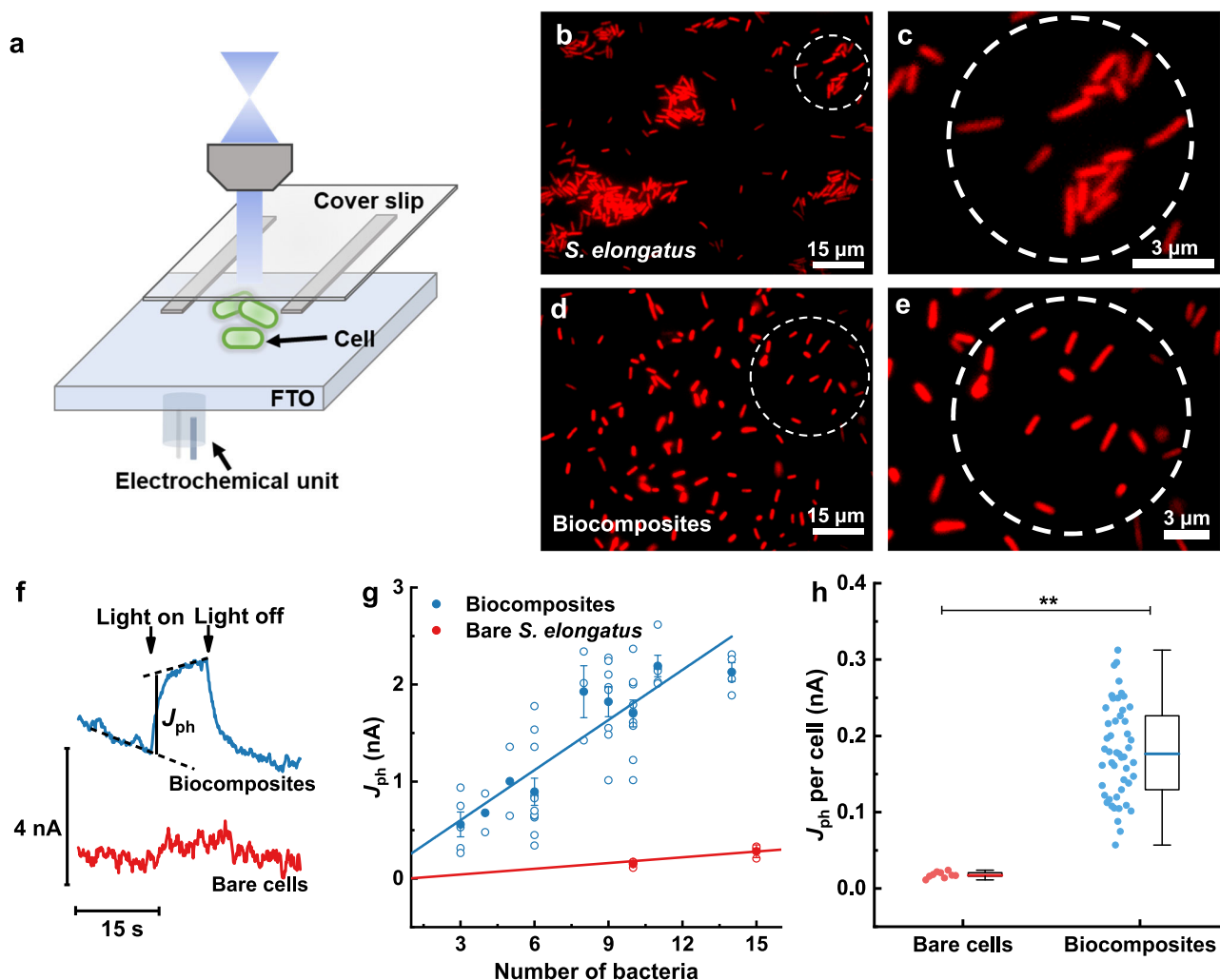
Fig. 5 | Multimodal imaging and photocurrent mapping of *S. elongatus* and PEDOT-S/*S. elongatus* biocomposites. a Schematic illustration of the multimodal imaging platform integrating a photoelectrochemical microfluidic cell with a fluorescence microscope. The setup utilizes multiple modulated lasers to enable both wide-field and focused excitation. The FTO working electrode is connected to a potentiostat for photoelectrochemical current mapping. **b**, **c** Fluorescence images of *S. elongatus* cells and the representative zoomed-in images of the regions indicated by dotted circles. Excitation at 405 nm, emission at 650–750 nm. **d**, **e** Fluorescence images of PEDOT-S/*S. elongatus* biocomposites and the representative zoomed-in images of the regions indicated by dotted circles. Each dotted area contains 15 bacteria. Scale bars indicate the magnification level. **f** Local current–time (*J*–*t*) profiles for bare *S. elongatus* (red curve) and PEDOT-S/*S. elongatus* biocomposites (blue curve) under a 405 nm light on-off cycle, corresponding to the regions in (**c**, **e**). **g** Plot of J_{ph} as a function of bacterial count for bare *S. elongatus* (red data points) and PEDOT-S/*S. elongatus* biocomposites (blue data points). The error bars represent the standard error of the mean. For bare *S. elongatus*, replicates (*n*) of 3, 2, and 3 for bacterial numbers of 10, 15, and 26, respectively. For PEDOT-S/*S. elongatus* biocomposites, replicates (*n*) of 5, 2, 2, 11, 3, 8, 9, 5, and 4 for bacterial numbers of 3, 4, 5, 6, 8, 9, 10, 11, and 14, respectively. **h** J_{ph} per cell for bare *S. elongatus* (red bars, *n* = 9) and PEDOT-S/*S. elongatus* biocomposites (blue bars, *n* = 49). Box plots show the distribution of the data: the center line indicates the median, the box bounds represent the lower to upper quartile values of the data, and the whiskers extend to the minimum and maximum values within 1.5× the interquartile range from the box. Individual data points in **g**, **h** represent both biological and technical replicates. Statistical analysis was performed using one-way ANOVA followed by Tukey's Honestly Significant Difference (HSD) post-hoc test. All tests were two-sided, and *p* values were adjusted for multiple comparisons. The p-value for the comparison between bare cells and biocomposites is 0.001 (*$p < 0.05$, **$p < 0.01$).

biocomposites (Supplementary Note 3), merging these methods may unlock opportunities for high-performance, scalable biophotovoltaic devices.

Discussion

In summary, we developed a photosynthetic 3D living biocomposite by integrating a self-doped conjugated polyelectrolyte PEDOT-S with the photoactive microorganism *S. elongatus*. The living biocomposite amplified the photocurrent output by more than 20-fold without a mediator relative to *S. elongatus* alone and by approximately 6-fold with a mediator present. Electrochemical characterization revealed that PEDOT-S enhanced interfacial electron transfer from *S. elongatus* cells to the electrode. Furthermore, the

photosynthetic function of the microorganism is maintained in the biocomposite under continuous illumination. Single-cell level experiments offer further insights into microscopic cell-electrode interactions facilitated by the PEDOT-S matrix. From a broader perspective, the approach presented here integrates the individual properties and advantages of both biotic and abiotic components, leveraging the natural photosynthetic capabilities of microorganisms and the characteristic electronic properties of conjugated polyelectrolytes. The potential applications of such biocomposites extend to various renewable energy technologies with the perspect of providing a sustainable solution for green energy generation. Meanwhile, single-cell experiments will bridge the gap between understanding individual cell behavior and applying it

to larger systems, driving innovation across bioelectrochemical technologies.

Methods

Culture of cyanobacterium *Synechococcus elongatus* PCC 7942

S. elongatus was purchased from Chemoscience Pte Ltd for this study. The concentration of the bacterial cells was quantified using a spectrophotometer to measure the optical density at 730 nm (OD_{730}). The cell culture medium, BG11, was prepared following the American Type Culture Collection (ATCC) guidelines, comprising $1.5 \, g \, L^{-1}$ $NaNO_3$, $0.04 \, g \, L^{-1}$ K_2HPO_4, $0.075 \, g \, L^{-1}$ $MgSO_4 \times 7H_2O$, $0.036 \, g \, L^{-1}$ $CaCl_2 \times 2H_2O$, $6.0 \, mg \, L^{-1}$ citric acid, $6.0 \, mg \, L^{-1}$ ferric ammonium citrate, $1.0 \, mg \, L^{-1}$ EDTA, $0.02 \, g \, L^{-1}$ Na_2CO_3, $1.0 \, mL$ Trace Metal Mix A5 containing $2.86 \, g \, L^{-1}$ H_3BO_3, $1.81 \, g \, L^{-1}$ $MnCl_2 \times 4H_2O$, $0.222 \, g \, L^{-1}$ $ZnSO_4 \times 7H_2O$, $0.039 \, g \, L^{-1}$ $Na_2MoO_4 \times 2H_2O$, $0.079 \, g \, L^{-1}$ $CuSO_4 \times 5H_2O$, $49.4 \, mg \, L^{-1}$ $Co(NO_3)_2 \times 6H_2O$. The pH of the medium is adjusted to 7.1 to minimize abiotic pseudo-photocurrent from manganese ions in weakly alkaline environments (pH -8)[15].

For culturing, a 10 mL aliquot of BG11 was sterilely inoculated with a cryopreserved stock of *S. elongatus* and revived under continuous white light illumination at $0.4 \, mW \, cm^{-2}$ (approximately 20 µmol photons $m^{-2} \, s^{-1}$), at a temperature of 30 °C within a 1% CO_2 environment. This preculture was then streaked onto BG11 agar plates and incubated at 30 °C for colony formation. Once colonies were confirmed on agar, a small portion of the biomass was inoculated into a liquid BG11 medium. The growth of these liquid cultures was regularly monitored by measuring their absorbance at 730 nm. Before biophotovoltaic experiments, a mild ethylenediaminetetraacetic acid (EDTA) treatment was conducted to remove extracellular polymeric substances (EPS) of *S. elongatus* to facilitate extracellular electron transfer[74–76]. Briefly, approximately 5 mg wet-cell-biomass mL^{-1} was mixed with an equal volume of 2% EDTA in BG11 medium and incubated at 4 °C for 3 h[77]. Subsequently, cultures were centrifuged at $5724 \times g$ for 5 mins and washed with fresh BG11 medium three times. The final cultures, adjusted to an OD_{730} of approximately 0.9 (equivalent to about 4.5×10^8 cells mL^{-1}), were used for further experimental studies involving photosynthetic activity and biophotovoltaic experiments.

Fabrication of microbial three-electrode electrochemical cell

As shown in Fig. S16, an ITO glass substrate with a size of 5×2.5 cm and with a sheet resistance of 6–8 Ω served as the working electrode in the setup. To define a precise active area for the electrochemical reactions, a rubber gasket was placed on the electrode surface, creating a confined region of 2 cm^2 with a depth of 600 µm. This ensured a consistent and controlled environment for the biocomposite interface.

Before the application of the biocomposite, the ITO electrodes underwent a thorough cleaning process and were treated with ultraviolet (UV) ozone to render the surface hydrophilic. This treatment removes organic contaminants and introduces hydroxyl groups onto the electrode surface, enhancing the adhesion of the biocomposite and ensuring intimate contact between the electrode and the PEDOT-S/*S. elongatus* layer. Subsequently, 100 µL of the PEDOT-S/*S. elongatus* biocomposite was carefully dispensed onto the defined working area of the ITO electrode. The biocomposite was evenly spread to form a uniform layer, which is crucial for reproducible electrochemical measurements and efficient wiring between the biological and electronic components. The same procedure is used to prepare bare *S. elongatus* samples.

To facilitate ion exchange and redox mediator transport while retaining the cells near the electrode, a dialysis membrane with a molecular weight cut-off (MWCO) of 3.5 kDa was placed over the biocomposite or liquid culture layer. The assembled electrochemical cell was filled with 15 mL of BG11 medium, incorporating 1 mM $K_3[Fe(CN)_6]$ to act as an electron transfer mediator. Carbon felt (area of 1 cm^2) and

an Ag/AgCl electrode (3 M KCl) were employed as counter and reference electrodes, respectively.

Bioelectrochemical experiments

Electrochemical measurements were performed using a VMP-300 potentiostat, Bio-Logic SAS, under 30 °C incubation, ambient air conditions. Chronoamperometry (CA) was performed at apotential (E_{CA}) of 0.3 V versus Ag/AgCl. Before monitoring the microbial photocurrent, the electrochemical cells were incubated in darkness for 3 hours to stabilize the system and eliminate residual capacitive currents. A white LED light (1 mW cm^{-2}, approximately 50 µmol photons $m^{-2} \, s^{-1}$) controlled by a timer switch was used to affect alternating dark and light conditions.

Cyclic voltammetry (CV) experiments were designed to characterize the electrochemical behaviors and electron transfer at the biocomposite-electrode interface. The working electrode potential was swept from an initial potential ($E_{initial}$) of −0.5 V to a vertex potential (E_{vertex}) of 0.6 V, and then returned to a final potential (E_{final}) of −0.5 V. This potential sweep was conducted at a scan rate of $0.005 \, V \, s^{-1}$.

In electrochemical impedance spectroscopy (EIS) experiments, the working electrode potential was maintained at a direct current (DC) potential (E_{DC}) of 0.3 V versus Ag/AgCl. A small sinusoidal alternating current (AC) potential with an amplitude (E_{AC}) of 5 mV was applied spanninga frequency range from 100 kHz down to 100 MHz. EIS data were analyzed using equivalent circuit models to extract parameters including charge transfer resistance and diffusion resistance.

Calculation of charge transfer resistance and restricted diffusion resistance

The charge transfer resistance (R_{CT}) and the restricted diffusion resistance (R_d) were determined following established literature protocols using an equivalent circuit model to fit the impedance spectra (Z) as a function of frequency (f)[59]. This model is represented by the equation:

$$Z(f) = R_s + \frac{R_{CT}}{Q} + Ma \tag{1}$$

In this model, all resistances indicated in the Nyquist plots are normalized by the area of the working electrode (2 cm^2). The solution resistance (R_S) in the Nyquist plot denotes the equivalent series resistance in $\Omega \, cm^{-2}$ and corresponds to the initial intersection with the real axis on the high-frequency side of the Nyquist plots. The R_{CT}, in $\Omega \, cm^{-2}$, is identified at the second intersection with the real axis in the midfrequency section of the plots. The element Q represents a constant phase element that accounts for potential deviations from an ideal capacitor.

Additionally, the presence of a finite space Warburg (FSW) impedance, indicated by a linear section terminating with an interfacial capacitor in the Nyquist plots, is modeled by the modified restricted diffusion element Ma, defined as:

$$Ma = R_d \frac{\coth\left(\sqrt[0.5a]{\tau j \omega}\right)}{\sqrt[0.5a]{\tau j \omega}} \tag{2}$$

Here R_d is the restricted diffusion resistance ($\Omega \, cm^{-2}$), τ is relaxation time (s) and Ω is angular frequency (rad s^{-1}). From this modeling, we can obtain the R_{CT} and R_d values for PEDOT-S and biocomposites. The fit quality was evaluated using the normalized Chi-squared ($\chi^2/|Z|$) value, with values lower than 0.01 indicating a reliable agreement between the experimental data and the model.

Scanning electron microscopy measurement

After the photoelectrochemical experiments, the medium in the electrochemical chambers was replaced with 4% glutaraldehyde prepared in fresh BG11 medium to fix the electrode-associated cells. The electrodes were incubated in this fixative solution for 24 hours at room temperature to ensure thorough fixation of the cellular structures. Following fixation, the electrodes were sequentially rinsed twice with BG11 medium and deionized water to remove residual glutaraldehyde and culture medium components.

Subsequent dehydration of the samples was performed using a graded ethanol series to gradually remove water while minimizing cellular distortion. The electrodes were immersed twice in 35% ethanol, followed by twice in 70% ethanol, each step lasting 1.5 hours. Finally, the electrodes were treated with 100% ethanol, with the first immersion lasting 1.5 hours and the second immersion extended overnight to ensure complete dehydration.

After dehydration, the electrodes underwent CO_2 critical point drying to prevent structural collapse during drying[45]. At the critical point, CO_2 transitions from liquid to gas phase without crossing a liquid–gas boundary, thus avoiding surface tension effects that can damage delicate structures or porosity in electrodes. This method preserves the microstructure of the biocomposites. Specifically, after disassembling the electrochemical cells, the working electrodes were gently rinsed with ethanol and then subjected to CO_2 critical point drying using a Leica EM CPD300 critical point dryer. The electrodes underwent sequential solvent exchange from ethanol to liquid CO_2. Once the chamber is filled with liquid CO_2 and all ethanol has been replaced, increase the temperature and pressure in the chamber to reach the critical point of CO_2 (31.1 °C, 7.38 MPa). The CO_2 gas was then slowly vented from the chamber, allowing the pressure to drop gradually to atmospheric levels while maintaining the chamber above the critical temperature. Finally, the dried electrodes were stored under inert atmosphere to avoid moisture uptake.

The dried electrodes were sputter-coated with a thin layer of platinum using an Anatech Hummer Sputtering System to enhance electrical conductivity and reduce charging effects during imaging. Scanning electron microscopy (SEM) imaging was conducted using a Hitachi FlexSEM1000. Imaging parameters were set with an accelerating voltage of 5 kV, a working distance of approximately 6 mm, and a beam current of 80 pA. Secondly, electron detection mode was employed to obtain high-resolution images of the microstructures of the PEDOT-S/*S. elongatus* biocomposites.

Confocal laser scanning microscopy

The microstructure and spatial distribution of *S. elongatus* cells within the PEDOT-S/*S. elongatus* biocomposites on ITO glass electrodes were examined using a confocal laser scanning microscope (Olympus FV3000). A ×60 oil immersion objective lens was utilized to image the samples. The intrinsic red fluorescence of chlorophyll within the *S. elongatus* cells was captured by exciting the samples at a wavelength of 620 nm and collecting emissions between 650 and 750 nm.

To investigate the three-dimensional architecture of the biocomposites, z-stack imaging was performed over a depth of 30 µm. This approach allowed for the reconstruction of the biocomposite structure along the z-axis, providing insights into the distribution and integration of *S. elongatus* cells within the PEDOT-S matrix. Image acquisition parameters were carefully optimized to minimize photobleaching and ensure an accurate representation of the cellular structures.

The acquired image stacks were processed and analyzed using Imaris Viewer software. This software facilitated three-dimensional visualization, rendering, and quantitative analysis of the cell distribution within the biocomposites.

Single-cell multimodal microscopy platform setup

The bacterial-cluster photocurrent measurement is based on an inverted microscope equipped with epifluorescence illumination and a customized three-electrode photoelectrochemical microfluidic cell. A 405 nm laser beam was expanded 15-fold using a beam expander (Thorlabs, GBE15-A), reflected by 425 nm long-pass dichroic mirror (Thorlabs, DMLP425R) and subsequently focused through a ×60 water immersion objective lens (Olympus, UPLSAPO60XW). An adjustable iris was positioned at the back port of the microscope, before focusing the light onto the back aperture of the objective, to precisely control the illuminated area. This setup enabled selective excitation of specific regions containing only a few isolated *S. elongatus* or PEDOT-S/*S. elongatus* biocomposites, facilitating the measurement of photocurrents originating exclusively from these targeted bacterial clusters. The illumination area was defined by a laser spot with a diameter of approximately 10–20 µm and a power density of 8.18 W cm^{-2}. The number of bacteria within the illuminated area was determined by detecting their intrinsic fluorescence, which was filtered through a 700 ± 25 nm emission filter (Edmund) and captured using a scientific Complementary Metal–Oxide–Semiconductor (sCMOS) camera (ANDOR SONA). The imaging process was controlled by ANDOR SOLIS software.

In the customized three-electrode photoelectrochemical microfluidic cell, FTO electrodes were used as the substrate, onto which 1–2 µL of either bare *S. elongatus* or PEDOT-S/*S. elongatus* biocomposites were deposited. These were subsequently covered with an agarose pad approximately 100 µm thick to ensure close contact between the bacteria and the electrode. BG11 medium containing 1 mM $K_3Fe(CN)_6$ was introduced into the microfluidic cell using a syringe pump (Chemyx Incorporation), after which the flow was halted to prevent disturbances in the current. The FTO electrode with the deposited cells acted as the working electrode, controlled by a potentiostat (Bio-Logic SP 300), while a platinum wire and an Ag/AgCl electrode served as the counter and reference electrodes, respectively. Chronoamperometric measurements were performed at 0.5 V during light on–off cycles, typically 10 seconds of illumination followed by 20 seconds of darkness, repeated over five cycles. The resulting current-time (*i-t*) responses were recorded. To quantify the photocurrent, the currents before and after the onset of illumination were fitted with linear functions. The difference between these fitted functions at the time point was used to determine the photocurrent for each light on/off cycle.

Compared to 0.3 V applied in bulk experiments, the use of 0.5 V in single-cell photocurrent mapping is mainly for enhancing sensitivity and improving signal-to-noise ratio. Single-cell measurements inherently produce much smaller currents compared to bulk measurements due to the limited number of cells contributing to the signal. To reliably detect these low current signals, a higher applied potential is necessary to increase the driving force for electron transfer and help to distinguish the photocurrent generated by individual cells from the background noise and capacitive currents.

Statistics analysis

Results are presented as mean ± standard error of the mean (SEM) taken from distince samples ($n \geq 3$) unless otherwise stated. Statistical analysis was performed using one-way ANOVA followed by Tukey's Honestly Significant Difference (HSD) post-hoc test. Asterisk (*) denotes statistical significance between bars (**$P < 0.01$, and *$P < 0.05$). The values of $P < 0.01$ were considered to be statistically significant. The statistical analyses and graphs were performed using OriginLab 2018.

Reporting summary

Further information on research design is available in the Nature Portfolio Reporting Summary linked to this article.

Data availability
All data underlying this study are available from the corresponding author upon request.

References

1. McCormick, A. J. et al. Biophotovoltaics: oxygenic photosynthetic organisms in the world of bioelectrochemical systems. *Energ. Environ. Sci.* **8**, 1092–1109 (2015).
2. Lawrence, J. M. et al. Rewiring photosynthetic electron transport chains for solar energy conversion. *Nat. Biomed. Eng.* **1**, 887–905 (2023).
3. Pisciotta, J. M., Zou, Y. & Baskakov, I. V. Light-dependent electrogenic activity of cyanobacteria. *PLoS One* **5**, e10821 (2010).
4. Grattieri, M. Purple bacteria photo-bioelectrochemistry: enthralling challenges and opportunities. *Photochem. Photobiol. Sci.* **19**, 424–435 (2020).
5. Buscemi, G. et al. Bio-inspired redox-adhesive polydopamine matrix for intact bacteria biohybrid photoanodes. *ACS Appl. Mater. Interfaces* **14**, 26631–26641 (2022).
6. Zhang, J. Z. et al. Photoelectrochemistry of photosystem ii in vitro vs in vivo. *J. Am. Chem. Soc.* **140**, 6–9 (2018).
7. Wey, L. T. et al. A biophotoelectrochemical approach to unravelling the role of cyanobacterial cell structures in exoelectrogenesis. *Electrochim. Acta* **395**, 139214 (2021).
8. Kornienko, N., Zhang, J. Z., Sakimoto, K. K., Yang, P. & Reisner, E. Interfacing nature's catalytic machinery with synthetic materials for semi-artificial photosynthesis. *Nat. Nanotechnol.* **13**, 890–899 (2018).
9. Wey, L. T. et al. The development of biophotovoltaic systems for power generation and biological analysis. *ChemElectroChem* **6**, 5375–5386 (2019).
10. Torquato, L. Dd. M. & Grattieri, M. Photobioelectrochemistry of intact photosynthetic bacteria: Advances and future outlook. *Curr. Opin. Electroche.* **34**, 101018 (2022).
11. Fang, X., Kalathil, S. & Reisner, E. Semi-biological approaches to solar-to-chemical conversion. *Chem. Soc. Rev.* **49**, 4926–4952 (2020).
12. Saar, K. L. et al. Enhancing power density of biophotovoltaics by decoupling storage and power delivery. *Nat. Energy* **3**, 75–81 (2018).
13. Zou, Y., Pisciotta, J. & Baskakov, I. V. Nanostructured polypyrrole-coated anode for sun-powered microbial fuel cells. *Bioelectrochemistry* **79**, 50–56 (2010).
14. Zhu, H., Wang, H., Zhang, Y. & Li, Y. Biophotovoltaics: recent advances and perspectives. *Biotechnol. Adv.* **64**, 108101 (2023).
15. Kusama, S. et al. Order-of-magnitude enhancement in photocurrent generation of Synechocystis sp. PCC 6803 by outer membrane deprivation. *Nat. Commun.* **13**, 3067 (2022).
16. Sure, S. et al. Inquisition of Microcystis aeruginosa and Synechocystis nanowires: characterization and modelling. *Antonie Van Leeuwenhoek* **108**, 1213–1225 (2015).
17. Saper, G. et al. Live cyanobacteria produce photocurrent and hydrogen using both the respiratory and photosynthetic systems. *Nat. Commun.* **9**, 2168 (2018).
18. Zhu, H. et al. Development of a longevous two-species biophotovoltaics with constrained electron flow. *Nat. Commun.* **10**, 4282 (2019).
19. Tschortner, J., Lai, B. & Kromer, J. O. Biophotovoltaics: green power generation from sunlight and water. *Front. Microbiol.* **10**, 866 (2019).
20. Grattieri, M., Beaver, K., Gaffney, E. M., Dong, F. & Minteer, S. D. Advancing the fundamental understanding and practical applications of photo-bioelectrocatalysis. *Chem. Commun.* **56**, 8553–8568 (2020).
21. Longatte, G. et al. Investigation of photocurrents resulting from a living unicellular algae suspension with quinones over time. *Chem. Sci.* **9**, 8271–8281 (2018).
22. Clifford, E. R. et al. Phenazines as model low-midpoint potential electron shuttles for photosynthetic bioelectrochemical systems. *Chem. Sci.* **12**, 3328–3338 (2021).
23. Weliwatte, N. S., Grattieri, M. & Minteer, S. D. Rational design of artificial redox-mediating systems toward upgrading photo-bioelectrocatalysis. *Photochem. Photobiol. Sci.* **20**, 1333–1356 (2021).
24. Baikie, T. K. et al. Photosynthesis re-wired on the pico-second timescale. *Nature* **615**, 836–840 (2023).
25. Bombelli, P. et al. Quantitative analysis of the factors limiting solar power transduction by synechocystis sp. PCC 6803 in biological photovoltaic devices. *Energ. Environ. Sci.* **4**, 4690–4698 (2011).
26. Liu, Y. & Atanassov, P. Charge transfer at biotic/abiotic interfaces in biological electrocatalysis. *Curr. Opin. Electrochem.* **19**, 175–183 (2020).
27. Herrero-Medina, Z. et al. A biophotoelectrode based on boronic acid-modified Chlorella vulgaris cells integrated within a redox polymer. *Bioelectrochemistry* **146**, 108128 (2022).
28. Grattieri, M., Patterson, S., Copeland, J., Klunder, K. & Minteer, S. D. Purple bacteria and 3d redox hydrogels for bioinspired photo-bioelectrocatalysis. *ChemSusChem* **13**, 230–237 (2020).
29. Çevik, E., Titiz, M. & Şenel, M. Light-dependent photocurrent generation: novel electrochemical communication between biofilm and electrode by ferrocene cored Poly(amidoamine) dendrimers. *Electrochim. Acta* **291**, 41–48 (2018).
30. Antonucci, A. et al. Carbon nanotube uptake in cyanobacteria for near-infrared imaging and enhanced bioelectricity generation in living photovoltaics. *Nat. Nanotechnol.* **17**, 1111–1119 (2022).
31. Zhou, X. et al. Conducting polymers–thylakoid hybrid materials for water oxidation and photoelectric conversion. *Adv. Electron. Mater.* **5**, 1800789 (2018).
32. Zeng, Y. et al. Photoactive conjugated polymer-based hybrid biosystems for enhancing cyanobacterial photosynthesis and regulating redox state of protein. *Adv. Funct. Mater.* **31**, 2007814 (2020).
33. Zhou, X., Zeng, Y., Lv, F., Bai, H. & Wang, S. Organic semiconductor-organism interfaces for augmenting natural and artificial photosynthesis. *Acc. Chem. Res.* **55**, 156–170 (2022).
34. Roullier, C., Reggente, M., Gilibert, P. & Boghossian, A. A. Polypyrrole electrodes show strain-specific enhancement of photocurrent from cyanobacteria. *Adv. Mater. Technol.* **8**, 2201839 (2023).
35. Furukawa, Y., Moriuchi, T. & Morishima, K. Design principle and prototyping of a direct photosynthetic/metabolic biofuel cell (DPMFC). *J. Micromech. Microeng.* **16**, S220–S225 (2006).
36. Bombelli, P. et al. Surface morphology and surface energy of anode materials influence power outputs in a multi-channel mediatorless bio-photovoltaic (BPV) system. *Phys. Chem. Chem. Phys.* **14**, 12221–12229 (2012).
37. Reggente, M. et al. Polydopamine-coated photoautotrophic bacteria for improving extracellular electron transfer in living photovoltaics. *Nano Res.* **17**, 866–874 (2024).
38. Reggente, M., Politi, S., Antonucci, A., Tamburri, E. & Boghossian, A. A. Design of optimized PEDOT-based electrodes for enhancing performance of living photovoltaics based on phototropic bacteria. *Adv. Mater. Technol.* **5**, 1900931 (2020).
39. Wey, L. T. et al. Optoelectronic enhancement of photocurrent by cyanobacteria on sustainable AP-VPP-fabricated PEDOT electrodes. *Electrochim. Acta* **475**, 143597 (2024).
40. Méhes, G. et al. Solar heat-enhanced energy conversion in devices based on photosynthetic membranes and PEDOT:PSS-nanocellulose electrodes. *Adv. Sustain. Sys.* **4**, 1900100 (2019).
41. Kim, Y. J. et al. 3D printing of thylakoid-PEDOT:PSS composite electrode for bio-photoelectrochemical cells. *ACS Appl. Energ. Mater.* **6**, 773–781 (2023).

42. Anam, M., Gomes, H. I., Rivers, G., Gomes, R. L. & Wildman, R. Evaluation of photoanode materials used in biophotovoltaic systems for renewable energy generation. *Sustain. Energ. Fuels* **5**, 4209–4232 (2021).

43. Fang, X. et al. Structure-activity relationships of hierarchical three-dimensional electrodes with photosystem ii for semiartificial photosynthesis. *Nano Lett.* **19**, 1844–1850 (2019).

44. Chen, X. et al. 3D-printed hierarchical pillar array electrodes for high-performance semi-artificial photosynthesis. *Nat. Mater.* **21**, 811–818 (2022).

45. McCuskey, S. R., Su, Y., Leifert, D., Moreland, A. S. & Bazan, G. C. Living bioelectrochemical composites. *Adv. Mater.* **32**, e1908178 (2020).

46. McCuskey, S. R. et al. Current progress of interfacing organic semiconducting materials with bacteria. *Chem. Rev.* **122**, 4791–4825 (2022).

47. Cui, Q. & Bazan, G. C. Narrow band gap conjugated polyelectrolytes. *Acc. Chem. Res.* **51**, 202–211 (2018).

48. Quek, G., Vazquez, R. J., McCuskey, S. R., Kundukad, B. & Bazan, G. C. Enabling electron injection for microbial electrosynthesis with n-type conjugated polyelectrolytes. *Adv. Mater.* **34**, e2203480 (2022).

49. McCuskey, S. R. et al. Evolving synergy between synthetic and biotic elements in conjugated polyelectrolyte/bacteria composite improves charge transport and mechanical properties. *Adv. Sci.* **11**, e2405242 (2024).

50. Yano, H., Kudo, K., Marumo, K. & Okuzaki, H. Fully soluble self-doped poly(3,4-ethylenedioxythiophene) with an electrical conductivity greater than 1000 S cm^{-1}. *Sci. Adv.* **5**, eaav9492 (2019).

51. Mousa, A. H. et al. Method matters: exploring alkoxysulfonate-functionalized poly(3,4-ethylenedioxythiophene) and its unintentional self-aggregating copolymer toward injectable bioelectronics. *Chem. Mater.* **34**, 2752–2763 (2022).

52. Mai, C. K. et al. Facile doping of anionic narrow-band-gap conjugated polyelectrolytes during dialysis. *Angew. Chem. Int. Ed.* **52**, 12874–12878 (2013).

53. Cao, D. X. et al. The importance of sulfonate to the self-doping mechanism of the water-soluble conjugated polyelectrolyte PCPDTBT-SO3K. *Mater. Chem. Front.* **4**, 3556–3566 (2020).

54. Nguyen-Dang, T. et al. Dual-mode organic electrochemical transistors based on self-doped conjugated polyelectrolytes for reconfigurable electronics. *Adv. Mater.* **34**, 2270170 (2022).

55. Quek, G., Roehrich, B., Su, Y., Sepunaru, L. & Bazan, G. C. Conjugated polyelectrolytes: underexplored materials for pseudocapacitive energy storage. *Adv. Mater.* **34**, e2104206 (2022).

56. Kirchhofer, N. D., McCuskey, S. R., Mai, C. K. & Bazan, G. C. Anaerobic respiration on self-doped conjugated polyelectrolytes: impact of chemical structure. *Angew. Chem. Int. Ed.* **56**, 6519–6522 (2017).

57. Bryant, D. A. & Canniffe, D. P. How nature designs light-harvesting antenna systems: design principles and functional realization in chlorophototrophic prokaryotes. *J. Phys. B: At. Mol. Opt. Phys.* **51**, 033001 (2018).

58. Danielsen, S. P. O. et al. Mixed conductive soft solids by electrostatically driven network formation of a conjugated polyelectrolyte. *Chem. Mater.* **30**, 1417–1426 (2018).

59. Jiang, Y. et al. Recyclable conjugated polyelectrolyte hydrogels for pseudocapacitor fabrication. *ACS Appl. Mater. Interfaces* **16**, 19968–19976 (2024).

60. Vázquez, R. J. et al. Increasing the molecular weight of conjugated polyelectrolytes improves the electrochemical stability of their pseudocapacitor gels. *J. Mater. Chem. A* **10**, 21642–21649 (2022).

61. Zajdel, T. J. et al. PEDOT:PSS-based multilayer bacterial-composite films for bioelectronics. *Sci. Rep.* **8**, 15293 (2018).

62. Liu, X., Inda, M. E., Lai, Y., Lu, T. K. & Zhao, X. Engineered living hydrogels. *Adv. Mater.* **34**, e2201326 (2022).

63. Latonen, R. M. et al. Electrospinning of electroconductive water-resistant nanofibers of PEDOT-PSS, cellulose nanofibrils and PEO: fabrication, characterization, and cytocompatibility. *ACS Appl. Bio. Mater.* **4**, 483–493 (2021).

64. Laschuk, N. O., Easton, E. B. & Zenkina, O. V. Reducing the resistance for the use of electrochemical impedance spectroscopy analysis in materials chemistry. *RSC Adv.* **11**, 27925–27936 (2021).

65. Yip, B. R. P. et al. Conjugated polyelectrolyte thin films for pseudocapacitive applications. *Adv. Mater.* **36**, e2308631 (2024).

66. Karikalan, N., Karthik, R., Chen, S. M. & Chen, H. A. A voltammetric determination of caffeic acid in red wines based on the nitrogen doped carbon modified glassy carbon electrode. *Sci. Rep.* **7**, 45924 (2017).

67. Vázquez, R. J. et al. Pseudocapacitive gels based on conjugated polyelectrolytes: thickness and ion diffusion limitations. *J. Mater. Chem. A* **11**, 18843–18852 (2023).

68. Paulsen, B. D., Tybrandt, K., Stavrinidou, E. & Rivnay, J. Organic mixed ionic-electronic conductors. *Nat. Mater.* **19**, 13–26 (2020).

69. Zhao, F., Ruff, A., Rogner, M., Schuhmann, W. & Conzuelo, F. Extended operational lifetime of a photosystem-based bioelectrode. *J. Am. Chem. Soc.* **141**, 5102–5106 (2019).

70. Liu, L. & Choi, S. Self-sustainable, high-power-density bio-solar cells for lab-on-a-chip applications. *Lab Chip* **17**, 3817–3825 (2017).

71. Fu, B. et al. Single-cell multimodal imaging uncovers energy conversion pathways in biohybrids. *Nat. Chem.* **15**, 1400–1407 (2023).

72. Zou, Y., Pisciotta, J., Billmyre, R. B. & Baskakov, I. V. Photosynthetic microbial fuel cells with positive light response. *Biotechnol. Bioeng.* **104**, 939–946 (2009).

73. Wenzel, T., Hartter, D., Bombelli, P., Howe, C. J. & Steiner, U. Porous translucent electrodes enhance current generation from photosynthetic biofilms. *Nat. Commun.* **9**, 1299 (2018).

74. Kouzuma, A., Oba, H., Tajima, N., Hashimoto, K. & Watanabe, K. Electrochemical selection and characterization of a high current-generating *Shewanella oneidensis* mutant with altered cell-surface morphology and biofilm-related gene expression. *BMC Microbiol.* **14**, 190 (2014).

75. Gao, L. et al. Mediation of extracellular polymeric substances in microbial reduction of hematite by Shewanella oneidensis MR-1. *Front. Microbiol.* **10**, 575 (2019).

76. Wey, L. T. et al. Fourfold increase in photocurrent generation of *Synechocystis sp.* PCC 6803 by exopolysaccharide deprivation. *Electrochim. Acta* **497**, 144555 (2024).

77. Cao, B. et al. Extracellular polymeric substances from *Shewanella sp. HRCR-1* biofilms: characterization by infrared spectroscopy and proteomics. *Environ. Microbiol.* **13**, 1018–1031 (2011).

Acknowledgements

Author contributions

Z.C., S.R.M. and G.C.B. designed and optimized the concept of this project. Z.C., S.R.M., G.Q., Y.J. and D.O. performed and analyzed the bulk electrochemical measurements. Z.C. and B.R.P.Y. designed and synthesized the material. Z.C., S.R.M., G.Q. and S.O. cultured the *S. elongatus*. W.Z. and X.M. conducted and analyzed the single-cell multimodal microscopy. B.K. conducted the rheological measurement. Z.C. and S.R.M. wrote the original draft of this manuscript. All authors contributed to the review and revision of the manuscript.

Competing interests

The authors declare no competing interests.

Additional information

Supplementary information The online version contains supplementary material available at
https://doi.org/10.1038/s41467-025-61086-5.

Correspondence and requests for materials should be addressed to Guillermo C. Bazan.

Peer review information *Nature Communications* thanks Massimo Trotta, Laura Wey, Huawei Zhu and the other, anonymous, reviewers for their contribution to the peer review of this work. A peer review file is available.

Reprints and permissions information is available at
http://www.nature.com/reprints

Publisher's note Springer Nature remains neutral with regard to jurisdictional claims in published maps and institutional affiliations.

¹Institute for Functional Intelligent Materials (I-FIM), National University of Singapore, Singapore, Singapore. ²Institute for Digital Molecular Analytics and Science (IDMxS), Nanyang Technological University, Singapore, Singapore. ³Singapore Centre for Environmental Life Sciences Engineering (SCELSE), Nanyang Technological University, Singapore, Singapore. ⁴Department of Materials Science and Engineering, National University of Singapore, Singapore, Singapore. ⁵Centre for Hydrogen Innovations, National University Singapore, Singapore, Singapore. ⁶Synthetic Biology for Clinical and Technological Innovation (SynCTI), National University of Singapore, Singapore, Singapore. ⁷These authors contributed equally: Zhongxin Chen, Samantha R. McCuskey. ✉e-mail: chmbgc@nus.edu.sg